INTERNATIONAL JOURNAL FOR NUMERICAL METHODS IN FLUIDS
Int. J. Numer. Meth. Fluids 2008; **56**:37–62
Published online 6 June 2007 in Wiley InterScience (www.interscience.wiley.com). DOI: 10.1002/fld.1530

Completeness, conservation and error in SPH for fluids

G. L. Vaughan[1,*,†], T. R. Healy[2], K. R. Bryan[2], A. D. Sneyd[3] and R. M. Gorman[4]

[1]*Department of Maths, University of Otago, P.O. Box 56, Dunedin, New Zealand*
[2]*Department of Earth Sciences, University of Waikato, Private Bag 3105, Hamilton, New Zealand*
[3]*Department of Maths, University of Waikato, Private Bag 3105, Hamilton, New Zealand*
[4]*National Institute of Water and Atmospheric Research, P.O. Box 11115, Hamilton, New Zealand*

SUMMARY

Smoothed particle hydrodynamics (SPH) is becoming increasingly common in the numerical simulation of complex fluid flows and an understanding of the errors is necessary. Recent advances have established techniques for ensuring completeness conditions (low-order polynomials are interpolated exactly) are enforced when estimating property gradients, but the consequences on errors have not been investigated. Here, we present an expression for the error in an SPH estimate, accounting for completeness, an expression that applies to SPH generally. We revisit the derivation of the SPH equations for fluids, paying particular attention to the conservation principles. We find that a common method for enforcing completeness violates a property required of the kernel gradients, namely that gradients with respect the two position variables be equal and opposite. In such models this means conservation principles are not enforced and we present results that show this. As an aside we show the summation interpolant for density is a solution of, and may be used in the place of, the discretized, symmetrized continuity equation. Finally, we examine two examples of discretization errors, namely numerical boundary layers and the existence of crystallized states. Copyright © 2007 John Wiley & Sons, Ltd.

Received 5 December 2006; Revised 4 April 2007; Accepted 20 April 2007

KEY WORDS: SPH; smoothed particle hydrodynamics; conservation principles; completeness; error; fluids

1. INTRODUCTION

Complex free surface fluid flows are important in many areas in engineering and science. With the power of computers available today it has become feasible to simulate these processes numerically. The gridded Eulerian methods that have become ubiquitous in computational fluid dynamics (CFD) are natural candidates for such applications because they are well understood and source

*Correspondence to: G. L. Vaughan, Department of Mathematics and Statistics, University of Otago, P.O. Box 56, Dunedin, New Zealand.
†E-mail: glv@maths.otago.ac.nz

codes are common. Lagrangian particle-based methods are relative newcomers to the stable of numerical methods and it is appropriate to consider whether they offer better performance for such tasks.

In Lagrangian particle-based techniques the model domain is discretized by defining control masses which are often called particles. Such models must use the Lagrangian formulation, in which the motion of the particles is accounted for, when changes in the fluid properties are determined. When calculating the gradients of properties there is no stationary mesh to refer to and so the methods are called 'meshless' or 'meshfree'. Smoothed particle hydrodynamics (SPH) is one of the earliest examples of a meshless method [1, 2], but it is predated by the generalized finite difference method by a number of years [3]. The first application of a meshfree method to free surface fluid flows was conducted by Monaghan [4] using SPH and was followed by the SPH variant moving particle semi-implicit (MPS) [5]. The generalized finite difference method has also been applied to fluid flows, notably by Tang *et al.* [6], who simulated 3-d blood flow in deformable arteries.

The model of Monaghan [4] was used to simulate breaking waves, among other things, but at relatively low resolutions. Koshizuka *et al.* [5] also used their MPS model to simulate breaking waves, at comparable resolutions to Monaghan's simulations, and experienced similar problems, in particular flows had rough-free surfaces. Bonet and Lok [7] and Bonet *et al.* [8] created SPH models in which first-order completeness was enforced, meaning that first-order polynomials are reproduced exactly. Their simulations showed remarkable reductions in noise with smooth-free surfaces and regular particle distributions.

Monaghan [9] estimated the error in an SPH interpolant, but failed to account for the lack of completeness that SPH interpolants typically experience [10]. An expression for the total error in which the order of completeness is accounted for has not yet been given in the literature. This expression would be of some value since it determines how simulation parameters should be chosen. In correcting their SPH mode for completeness, Bonet *et al.* [8] used modified kernel gradients, but with the standard SPH equations. The problem with this approach is that modified kernels no longer have the property that gradients with respect to their two position arguments are equal and opposite, a property required of kernels in these equations. In this work, we say a kernel satisfying this condition is anti-symmetric in its gradient operators. The failure to meet this condition results in the failure to satisfy the conservation principles.

Here, we demonstrate how the SPH equation for mass conservation may be derived, showing how the condition of anti-symmetric gradient operators for kernels arises, and why it results in the failure to satisfy conservation principles if it is not met. We present results from simulations that show this non-conservation. In some SPH models, rather than discretizing the continuity equation, mass conservation is enforced by employing the summation interpolant (an equation that can be used to approximate an integral using disordered points) for the density. We review the justifications for this decision, making particular reference to the distinction between local and global conservation of mass. We show that the replacement is justified, because it is a solution to the discretized continuity equation.

Originating at the smallest scale within a simulation are two forms of error in SPH that result in large-scale artefacts, namely crystallized states [11] and numerical boundary layers [4]. To demonstrate this we present results from a simulation of a seiching basin in which a large stagnant layer is visible. We note that while boundary layers have been observed in the past, an explanation for their existence has not yet been given. We provide an explanation for why boundary layers occur in SPH simulations, and moreover, present results showing how these layers can have additional

DOI: 10.1002/fld

negative consequences. In a simulation of a solitary wave breaking on a plane beach we observe a numerical boundary layer, and moreover, a jet within this layer. These layers may be avoided through appropriate choice of the kernel.

2. BASIC SPH THEORY

The summation interpolant is the basis for discretization in SPH and we begin this section with an analysis of the error in this quantity. We continue by examining the derivation of the SPH equations from the conservation principles.

2.1. Discretization and error in a summation interpolant

To examine the rate of convergence for a summation interpolant we first need an expression for the form of the error. We start by introducing the integral interpolant (indicated by the subscript I):

$$\psi_I(\mathbf{r}_a, t) = \int_V \psi(\mathbf{r}, t) W(\mathbf{r}_a, \mathbf{r}, h)\, \mathrm{d}\mathbf{r} \tag{1}$$

in which ψ is an unspecified fluid property, $\mathbf{r}_a$ is a position vector and $\mathbf{r}$ is a dummy position variable. The variables used in this expression are shown graphically in Figure 1. The volume element at $\mathbf{r}$ is d$\mathbf{r}$ and the variable of integration is $\mathbf{r}$. The domain V is a volume, area or line segment, depending on dimension. The kernel $W(\mathbf{r}_a, \mathbf{r}, h)$ is an arbitrary peaked function with width parameter h (named the smoothing length) and is non-zero only within its support, a subset of the total domain. Here, we consider only the case of uniform and time-invariant h. When the support is finite and small the kernel is said to have a compact support. Kernels are generally constructed to have this property to save on computations. An example of a common kernel is the

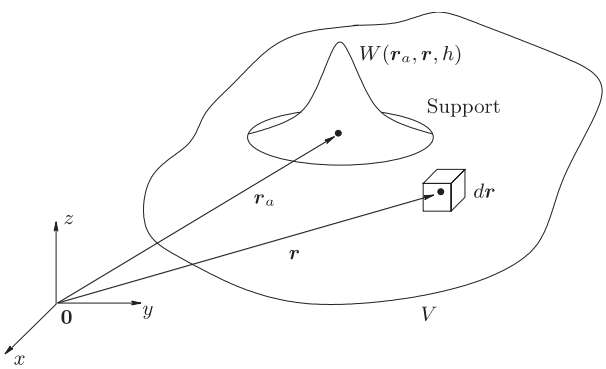

Figure 1. Notation used in this paper. The volume element at $\mathbf{r}$ is d$\mathbf{r}$ and while the support of the kernel at $\mathbf{r}_a$ is shown here to be a circle, it is actually a sphere in three dimensions (with radius $2h$ if Equation (2) is used).

DOI: 10.1002/fld

cubic spline [12]

$$W(q_a) = \frac{10}{7\pi h^2} \begin{cases} 1 - \frac{3}{2}q_a^2 + \frac{3}{4}q_a^3, & 0 \leqslant q_a \leqslant 1 \\ \frac{1}{4}(2 - q_a)^3, & 1 < q_a \leqslant 2 \\ 0, & 2 < q_a < \infty \end{cases} \tag{2}$$

in which $q_a = |\mathbf{u}_a|$ for $\mathbf{u}_a = (\mathbf{r}_a - \mathbf{r})/h$ and where the kernel has been normalized for two dimensions.

In the limit as $h \to 0$ the kernel has zero width and becomes a delta function. In this limit the integral interpolant is exact. The integral interpolant is still a continuous function and is discretized through approximating the integral to obtain the summation interpolant (indicated by the subscript S):

$$\psi_S(\mathbf{r}_a, t) = \sum_{b=1}^{M} \frac{m_b}{\rho_b} \psi(\mathbf{r}_b, t) W(\mathbf{r}_a, \mathbf{r}_b, h) \tag{3}$$

in which the summation is over the M disordered points within the support of the kernel and where ρ_b, $\mathbf{r}_b$ and m_b are the density, position and mass of fluid particle b. In the limit as $M \to \infty$ and $h \to 0$ the summation interpolant becomes exact. Note that in an SPH simulation the value of M may vary between particles and, for a single particle, it may also change with time. This means the error will vary in both space and time. In an SPH model, the errors may be quite large because $h > 0$ and M is small. In practise, we will reduce h and increase M until we have a solution for which the error is small enough.

2.1.1. The error in the summation interpolant. In approximating an integral using an SPH estimate an error is introduced. If the points are random, then the error is $O(M^{-1/2})$ [13], but in an SPH simulation points are not random. Monaghan [14] considers that in SPH simulations this estimate of the error does not converge quickly enough, and notes that if the estimate can be considered as being a quasi-Monte Carlo estimate then the error reduces as $O((\ln M)^{d-1}/M)$ [13]. Quasi-Monte Carlo estimates require that the domain be a unit cube in d dimensions and that the points be distributed in one of the special prescribed sequences [13] (a Halton sequence being an example). In SPH domains are rarely unit cubes (usually being spherical), and points are unlikely to occur in one of the prescribed sequences. Monaghan [9] conjectures that for initially regular particle distributions (presumably being close to one of the prescribed sequences) the errors are small, and reasons that they must remain so.

Exactly what the error is for a summation interpolant depends on the distribution of points. Quinlan *et al.* [15] recently used the Euler–MacLaurin formula to estimate this error for regular one-dimensional distributions, and their approach holds promise for the more difficult cases of higher dimension and increased disorder common in SPH. Until more work has been done examining the particle distributions that occur most frequently in SPH, it is not clear what form of error we should use. For simplicity, we use $O(f(M))$, so the error is $Cf(M)$ for C is an unknown but bounded constant.

We now derive an expression for the error in the summation interpolant. The approach used here is only slightly different to that existing in the literature [9], but it clearly shows the role of

DOI: 10.1002/fld

completeness. A Taylor expansion of $\psi(\mathbf{r}_b)$ about $\mathbf{r}_a$ in Equation (3) gives

$$\psi_S(\mathbf{r}_a,t)=\psi(\mathbf{r}_a,t)\sum_{b=1}^{M}\frac{m_b}{\rho_b}W(\mathbf{r}_a,\mathbf{r}_b,h)+\nabla_{r_a}^{\mathrm{T}}\psi(\mathbf{r}_a,t)\sum_{b=1}^{M}\frac{m_b}{\rho_b}(\mathbf{r}_a-\mathbf{r}_b)W(\mathbf{r}_a,\mathbf{r}_b,h)$$
$$+\frac{1}{2}\sum_{b=1}^{M}\frac{m_b}{\rho_b}(\mathbf{r}_a-\mathbf{r}_b)^{\mathrm{T}}H\psi(\boldsymbol{\xi},t)(\mathbf{r}_a-\mathbf{r}_b)W(\mathbf{r}_a,\mathbf{r}_b,h) \tag{4}$$

in which Lagrange's form for the remainder has been used so $\boldsymbol{\xi}$ lies in the support of the kernel at $\mathbf{r}_a$, and the superscript T shows the transpose has been taken. Here all vectors are column vectors. The matrix operator H is the Hessian matrix, so the ijth element is $\partial^2/\partial x_i\,\partial x_j$. Kernels are usually chosen so that they may be written as $W(\mathbf{r}_a,\mathbf{r}_b,h)=W(q_{ab})$ where $q_{ab}=|\mathbf{u}_{ab}|$ for $\mathbf{u}_{ab}=(\mathbf{r}_a-\mathbf{r}_b)/h$, and this is done here. The summations in Equation (4) can be recognized as the discretized forms of certain integrals, so

$$\psi_S(\mathbf{r}_a,t)=\psi(\mathbf{r}_a,t)\left(\int_{\hat{V}_a}W(q_a)\,\mathrm{d}\mathbf{u}_a+C_1'f(M)\right)$$
$$+\left(h\nabla_{r_a}^{\mathrm{T}}\psi(\mathbf{r}_a,t)\int_{\hat{V}_a}\mathbf{u}_aW(q_a)\,\mathrm{d}\mathbf{u}_a+C_2'hf(M)\right)$$
$$+\left(\frac{1}{2}h^2\int_{\hat{V}_a}\mathbf{u}_a^{\mathrm{T}}H\psi(\boldsymbol{\xi},t)\mathbf{u}_aW(q_a)\,\mathrm{d}\mathbf{u}_a+C_4'h^2f(M)\right) \tag{5}$$

where $\hat{V}_a$ is the volume of the support in $\mathbf{u}_a$-space, $\mathbf{u}_a$ is the variable of integration with volume element $\mathrm{d}\mathbf{u}_a$. Here C_1', C_2' and C_4' are constants with respect to h and M and the integrals have values that are independent of $\mathbf{r}_a$, h and M. At this point we place on the kernel the conditions that the first and second integrals appearing in Equation (5) (which are, respectively, the zeroth and first moments of the kernel) evaluate to 1 and $\mathbf{0}$, respectively. We also require the second moment of the kernel to have a finite value. If these requirements are satisfied then Equation (5) becomes

$$\psi_S(\mathbf{r}_a,t)=\psi(\mathbf{r}_a,t)(1+C_1'f(M))+(0+C_2'hf(M))+(C_3'h^2+C_4'h^2f(M)) \tag{6}$$

in which the C's are functions of ψ (and hence of $\mathbf{r}_a$ and t) and its derivatives but are constant with respect to M and h.

If we choose the kernel so that the estimates of the zeroth and first moments of the kernel are exact (essentially $C_1'=C_2'=0$) then the summation interpolant is first-order complete because it can approximate linear functions exactly. If only the estimate for the zeroth moment is exact (so only $C_1'=0$), then the summation interpolant is zeroth-order complete because it can approximate constants exactly. The use of the kernel given in Equation (2) does not result in either zeroth- or first-order completeness.

2.1.2. Convergence rates for summation interpolants. The number of points within the support of the kernel can be estimated from $M\approx CNh^d$, where d is the number of dimensions, N is the total number of points and C is a constant depending on the lengths, areas or volumes of the total

DOI: 10.1002/fld

Table I. The most significant errors in a summation interpolant, according to the order of completeness it achieves.

Order of completeness	Constants	Error	$N(h)$
Not zeroth	All non-zero	$O\left(\frac{1}{\sqrt{Nh^d}}\right)$	$N(h) \propto h^{-(2k+d)}$
Zeroth	$C_1 = 0$	$O\left(\frac{h}{\sqrt{Nh^d}}\right)$	$N(h) \propto h^{-(2k+d-2)}$
First	$C_1 = C_2 = 0$	$O\left(\frac{h^2}{\sqrt{Nh^d}}\right)$	$N(h) \propto h^{-(2k+d-4)}$

Note: The constants from Equation (7) that are zero are also shown for each case. The final column indicates how N (the total number of particles in the simulation) must be scaled with h to achieve convergence at the rate h^k, for $k \in 0, 1, 2$. For simplicity, we use $f(M) = 1/\sqrt{M}$ and $M \propto Nh^d$.

domain and the support. For the case of $f(M) = 1/\sqrt{M}$ (corresponding to points with a random distribution) Equation (6) becomes

$$\psi_S(\mathbf{r}_a, t) = \psi(\mathbf{r}_a, t) + \frac{C_1}{\sqrt{Nh^d}} + \frac{C_2 h}{\sqrt{Nh^d}} + C_3 h^2 + \frac{C_4 h^2}{\sqrt{Nh^d}} \tag{7}$$

where $C_i = C_i'/\sqrt{C}$ for $i \in \{2, 3, 4\}$ and $C_1 = C_1'\psi(\mathbf{r}_a, t)/\sqrt{C}$. The most significant term depends on the order of completeness that is achieved, and examples are given in Table I. This equation may be used to generate expressions for the form of $N(h)$ in order to achieve a desired convergence rate.

The expressions for $N(h)$ are of particular importance since they indicate how N must scale with h in order to achieve a convergence rate of h^k. We note that the error in the summation interpolant is dependent on the distribution of points, and that if the quasi-Monte Carlo error of $O((\ln M)^{d-1}/M)$ is used an analytic solution for $N(h)$ cannot be obtained.

We conclude this section by noting that summation interpolants can always converge provided N is chosen carefully for a given h, but that there is a trade off between convergence rate and computational workload. When completeness is not achieved the workload is very high.

2.1.3. Gradients from summation interpolants. Equation (6) gives the error in an SPH interpolant, however, in SPH the problem lies in estimating the gradients of properties. By using the identity

$$\nabla_r \psi(\mathbf{r}, t) W = \nabla_r(\psi(\mathbf{r}, t) W) - \psi(\mathbf{r}, t) \nabla_r W \tag{8}$$

and Gauss' theorem, the gradient in a function can be estimated from [12]

$$\int_V \nabla_r \psi(\mathbf{r}, t) W \, \mathrm{d}\mathbf{r} = \int_S \psi(\mathbf{r}, t) W \mathbf{n} \, \mathrm{d}S - \int_V \psi(\mathbf{r}, t) \nabla_r W \, \mathrm{d}\mathbf{r} \tag{9}$$

in which $W = W(\mathbf{r}_a, \mathbf{r}, h)$, S is the surface of V and has the surface element $\mathrm{d}S$ and outward pointing normal $\mathbf{n}$ at the point $\mathbf{r}$. We also have, for the divergence of a vector

$$\int_V \nabla_r \cdot \boldsymbol{\psi}(\mathbf{r}, t) W \, \mathrm{d}\mathbf{r} = \int_S \boldsymbol{\psi}(\mathbf{r}, t) \cdot \mathbf{n} W \, \mathrm{d}S - \int_V \boldsymbol{\psi}(\mathbf{r}, t) \cdot \nabla_r W \, \mathrm{d}\mathbf{r} \tag{10}$$

DOI: 10.1002/fld

SPH has been applied extensively to astrophysical problems, and in simulating these phenomena the assumption is made that either the function ψ or the kernel are zero on S. In applications of SPH to free surface fluid flows the same assumption has been applied, a step which introduces errors at the boundaries. We are not aware of any SPH models for free surface fluid flows in which surface integrals are included.

The kernel given in Equation (2) has an inflection point between the origin and the edge of the support. When Equations (9) and (10) are used with a kernel having such an inflection point, artificial clustering results [16], an effect that is closely related to the well-known tensile instability [17, 18]. This effect is manifested in a simulation as an unphysical cluster of closely packed particles surrounded by a region with too few particles. It comes about because at the inflection point there is a maximum in the gradient. Essentially, the force with which two particles repel one another reaches a maximum at that point, and then reduces as the particles are brought closer together. When it occurs artificial clustering is a significant source of error in SPH.

Methods have been developed in order to ensure estimates for property gradients are first-order complete. In one such method the kernel is modified so that for particle a the corrected gradient of the kernel at b is given by [8]

$$\tilde{\nabla}_{r_b} W(q_{ab}) = \mathbf{L}_a [\nabla_{r_b} W(q_{ab}) + \boldsymbol{\varepsilon}_a \delta_{ab}] \tag{11}$$

in which the summation convention does not apply. To use this correction method, the corrected kernel gradient replaces the uncorrected kernel gradient in the standard SPH equations. The matrix $\mathbf{L}_a$ and the vector $\boldsymbol{\varepsilon}_a \delta_{ab}$ (δ_{ab} is the Kronecker delta) are found by requiring that the zeroth- and first-order completeness conditions are satisfied.

In Section 2.2.2 the SPH equation for conservation of mass is derived and it is demonstrated that anti-symmetry of the gradient operators (∇_{r_a} and ∇_{r_b}, defined in Equation (16)) acting on the kernel is required. If the correction method described above is used this condition is violated. Uncorrected kernels usually obey $\nabla_{r_a} W(q_{ab}) = -\nabla_{r_b} W(q_{ab})$, a result of being chosen to be radially symmetric. The corrected kernel gradient does not obey this property because it has a factor that is a function of $\mathbf{x}_a$, rather than q_{ab}.

In addition, it is commonly asserted that the force of particle a acting on particle b is, in part, determined by the value of $\nabla_{r_a} W(q_{ab})$, and consequently Newton's third law requires $\nabla_{r_a} W(\mathbf{r}_a, \mathbf{r}_b, h) = -\nabla_{r_b} W(\mathbf{r}_b, \mathbf{r}_a, h)$ (note the order of the arguments). Clearly, when using this correction method this condition will only be satisfied if $\mathbf{L}_a = \mathbf{L}_b$, unlikely because it requires that the two particles have the same distributions of neighbours.

2.2. Conservation principles

All computational models for simulating fluids are based on the fundamental principles of physics [19, 20]. The principles of relevance here are the principles of conservation of mass, energy, momentum and angular momentum [20]. The principles of conservation of energy and angular momentum are not always used in CFD models, because they are not always independent of the other principles. For many applications the equations of conservation of momentum and mass represent an irreducible set.

Here, we make the distinction between local and global conservation. If a condition holds locally everywhere, then it holds at each and every point within a domain. The term global is used to describe a condition that applies to the entire system. If a condition is satisfied locally everywhere

DOI: 10.1002/fld

then it is also satisfied globally, but the converse is not true: a global condition being met does not mean that the corresponding local condition is satisfied.

2.2.1. The material derivative. Fundamental to the Lagrangian formulation used in particle-based methods is the material derivative

$$\frac{D\psi(\mathbf{r},t)}{Dt}=\frac{\partial\psi(\mathbf{r},t)}{\partial t}+\mathbf{v}(\mathbf{r},t)\cdot\nabla_r\psi(\mathbf{r},t) \tag{12}$$

which describes the time rate of change of ψ following the motion of the fluid where $\mathbf{v}$ is the velocity of the fluid. This is just the total derivative with respect to time evaluated at the Lagrangian point $\mathbf{r}$, a point for which $\mathrm{d}\mathbf{r}(t)/\mathrm{d}t=\mathbf{v}(\mathbf{r}(t),t)$. The partial derivative with respect to time in Equation (12) is evaluated with the spatial coordinates held constant.

2.2.2. Conservation of mass. The equation of conservation of mass can be written as

$$\frac{D\rho(\mathbf{r},t)}{Dt}=-\rho(\mathbf{r},t)\nabla_r\cdot\mathbf{v}(\mathbf{r},t) \tag{13}$$

If this differential equation is satisfied at every point $\mathbf{r}$ within the model domain, and irrespective of whether the system is closed or not, then mass is conserved locally everywhere.

SPH is almost always used with the constraint that the masses of particles must remain constant in time. This is most easily enforced by requiring that the boundaries of particles be Lagrangian, convected with the fluid, and so no mass flows over those boundaries. It may be shown that, by integrating Equation (13) over the volume $V_a(t)$ we have

$$\frac{\partial m_a}{\partial t}=0 \tag{14}$$

So for particles with Lagrangian boundaries, having constant mass is sufficient to enforce local conservation of mass. However, this does not provide the required information about the variable ρ, for which we need another expression.

In the following we derive the SPH equation usually used to enforce conservation of mass, a derivation that closely follows that of [9], but here we account for the time-dependent domain. We first multiply Equation (13) by the kernel $W=W(\mathbf{r}_a,\mathbf{r},h)$ and integrate over the domain:

$$\begin{aligned}\int_{V(t)}\frac{D\rho(\mathbf{r},t)}{Dt}W\,\mathrm{d}\mathbf{r}&=\int_{V(t)}\frac{\partial\rho(\mathbf{r},t)}{\partial t}W\,\mathrm{d}\mathbf{r}+\int_{V(t)}\mathbf{v}(\mathbf{r},t)\cdot\nabla_r\rho(\mathbf{r},t)W\,\mathrm{d}\mathbf{r}\\&=-\int_{V(t)}\rho(\mathbf{r},t)\nabla_r\cdot\mathbf{v}(\mathbf{r},t)W\,\mathrm{d}\mathbf{r}\end{aligned} \tag{15}$$

We note that the gradient operators ∇_r and ∇_{r_a} are defined by

$$\nabla_r=\frac{\partial}{\partial r_x}\mathbf{i}+\frac{\partial}{\partial r_y}\mathbf{j}+\frac{\partial}{\partial r_z}\mathbf{k}\quad\text{and}\quad\nabla_{r_a}=\frac{\partial}{\partial r_{ax}}\mathbf{i}+\frac{\partial}{\partial r_{ay}}\mathbf{j}+\frac{\partial}{\partial r_{az}}\mathbf{k} \tag{16}$$

In the first of these $\mathbf{r}_a$ and t are held constant, while in the second $\mathbf{r}$ and t are held constant. For the operator $\partial/\partial t$ both $\mathbf{r}_a$ and $\mathbf{r}$ are held constant. The dummy variable $\mathbf{r}$ is a position vector that

DOI: 10.1002/fld

takes on the values of all positions within the domain of the system, and as such, is independent of time. The operator ∇_{r_b} is similarly defined. The velocity of the point $\mathbf{r}_a$ is given by

$$\mathbf{v}(\mathbf{r}_a, t) = \frac{\mathrm{d}\mathbf{r}_a(t)}{\mathrm{d}t} \tag{17}$$

in which $\mathrm{d}/\mathrm{d}t$ is the total derivative with respect to time. Note that the position of the Lagrangian point $\mathbf{r}_a$ depends only on time.

By applying Equation (8) to the term $\rho(\mathbf{r}, t)\mathbf{v}(\mathbf{r}, t)$ appearing in Equation (15) we can write

$$\frac{\partial}{\partial t}\int_{V(t)} \rho(\mathbf{r}, t) W \,\mathrm{d}\mathbf{r} = -\int_{V(t)} \nabla_r \cdot [\rho(\mathbf{r}, t)\mathbf{v}(\mathbf{r}, t) W] \,\mathrm{d}\mathbf{r} + \int_{V(t)} \rho(\mathbf{r}, t)\mathbf{v}(\mathbf{r}, t) \cdot \nabla_r W \,\mathrm{d}\mathbf{r} + \int_{S(t)} \rho(\mathbf{r}, t) W \mathbf{v}(\mathbf{r}, t) \cdot \mathbf{n} \,\mathrm{d}S \tag{18}$$

in which the last integral occurs because [21, p. 439]

$$\frac{\partial}{\partial t}\int_{V(t)} \rho(\mathbf{r}, t) W \,\mathrm{d}\mathbf{r} = \int_{V(t)} \frac{\partial \rho(\mathbf{r}, t)}{\partial t} W \,\mathrm{d}\mathbf{r} + \int_{S(t)} \rho(\mathbf{r}, t) W \mathbf{v}(\mathbf{r}, t) \cdot \mathbf{n} \,\mathrm{d}S \tag{19}$$

a direct consequence of the time dependence of the domain. The vector $\mathbf{n}$ is the outward pointing normal vector on the surface element $\mathrm{d}S$ at $\mathbf{r}$. The first and third integrals on the right-hand side of Equation (18) cancel after an application of Gauss' theorem. Adding $\mathbf{v}(\mathbf{r}_a, t).\nabla_{r_a}\rho_I(\mathbf{r}_a, t)$ to each side gives

$$\frac{D\rho_I(\mathbf{r}_a, t)}{Dt} = \int_{V(t)} \rho(\mathbf{r}, t)[\mathbf{v}(\mathbf{r}_a, t) \cdot \nabla_{r_a} + \mathbf{v}(\mathbf{r}, t) \cdot \nabla_r] W \,\mathrm{d}\mathbf{r} \tag{20}$$

Most kernels are constructed so the kernel gradients obey $\nabla_r W = -\nabla_{r_a} W$ (the condition of anti-symmetric kernel gradient operators), so we get

$$\frac{D\rho_I(\mathbf{r}_a, t)}{Dt} = \int_{V(t)} \rho(\mathbf{r}, t)[\mathbf{v}(\mathbf{r}_a, t) - \mathbf{v}(\mathbf{r}, t)] \cdot \nabla_{r_a} W \,\mathrm{d}\mathbf{r} \tag{21}$$

A summation interpolant may be used to approximate the integral and the discretized continuity equation results:

$$\frac{D\rho_a}{Dt} = \sum_{b=1}^{N} m_b(\mathbf{v}_a - \mathbf{v}_b) \cdot \nabla_{r_a} W(q_{ab}) \tag{22}$$

in which $\rho_a = \rho(\mathbf{r}_a, t)$, $\mathbf{v}_a = \mathbf{v}(\mathbf{r}_a, t)$, the mass of particle b is m_b and N is the total number of particles in the system. The summation can be performed over N, rather than M, because for points not in the support the kernel gradient is zero.

This derivation was presented here to show how the condition of anti-symmetric kernel gradient operators comes about. In addition, we have shown that there are no boundary integrals when the continuity equation is discretized in SPH.

DOI: 10.1002/fld

2.2.3. Global conservation of mass. If global mass is conserved in a system then the difference between flows of mass into and out of the system are equal to the change in mass within the system. For a closed system no mass may enter or leave the system anywhere, neither over boundaries, nor through sources or sinks within the system. Local conservation of mass is a more stringent requirement, placing a condition on the divergence of the mass flux density ($\rho\mathbf{v}$) *via* the continuity equation.

It is relatively easy to show that (for a closed system) by integrating Equation (21) with respect to $\mathbf{r}$ over the entire domain we get, where M is the global mass

$$\frac{\partial M}{\partial t} = 0 \tag{23}$$

which is a statement of global conservation of mass. This was noted by Monaghan [9] who, incidentally, asserted that the continuity equation resulted in conservation of mass both globally and locally everywhere.

In traditional SPH the continuity equation is often replaced by the integral interpolant for the density

$$\rho_I(\mathbf{r}_a, t) = \int_{V(t)} \rho(\mathbf{r}, t) W(q_a)\, \mathrm{d}\mathbf{r} \tag{24}$$

which is discretized using Equation (3) to become the summation interpolant for the density. Either of the integral or summation interpolants for the density may be integrated over the entire domain to obtain $M = M$. Both Gingold and Monaghan [1] and also Lucy [2] assert that the $M = M$ means Equation (24) is equivalent to conservation of mass, but more correctly it is equivalent to global conservation of mass.

2.2.4. The summation interpolant for density. It turns out that the summation interpolant for density can still be legitimately used in SPH and will enforce local conservation of mass. Starting from the discretized continuity equation (22), we integrate from time t_1 to t_2 to obtain

$$\rho_a(t_2) - \rho_a(t_1) = \int_{t_1}^{t_2} \sum_{b=1}^{N} m_b \left[\frac{\mathrm{d}\mathbf{r}_a}{\mathrm{d}t} - \frac{\mathrm{d}\mathbf{r}_b}{\mathrm{d}t} \right] \nabla_{r_a} W(q_{ab})\, \mathrm{d}t \tag{25}$$

This becomes

$$\rho_a(t_2) - \rho_a(t_1) = \int_{t_1}^{t_2} \sum_{b=1}^{N} m_b \frac{\mathrm{d}W(q_{ab})}{\mathrm{d}t}\, \mathrm{d}t \tag{26}$$

We require the m_b to be constant with respect to time so the total derivative may be moved outside the summation and this becomes

$$\rho_a(t_2) - \rho_a(t_1) = \sum_{b=1}^{N} m_b W(q_{ab}) \Big|_{t_1}^{t_2} \tag{27}$$

If

$$\rho_a(t_1) = \sum_{b=1}^{N} m_b W(q_{ab}(t_1)) \tag{28}$$

DOI: 10.1002/fld

then

$$\rho_a(t_2) = \sum_{b=1}^{N} m_b W(q_{ab}(t_2)) \tag{29}$$

and so the summation interpolant for density satisfies the discretized continuity equation.

The low accuracy, Monaghan [4], observed using this expression is partly a result of the lack of completeness in the estimate. Correcting the summation interpolant for density for completeness would be a difficult task because of the existing requirement of anti-symmetric kernel gradient operators. If the summation interpolant for density is used then the error introduced is for the density, while if the discretized continuity equation is used the error is for the rate of change in the density, the latter error being much smaller.

2.2.5. Conservation of momentum. The equation of conservation of momentum can be discretized in a similar manner to that shown for discretizing the continuity equation, although the non-linear term requires some special attention [9]. The SPH equation for conservation of momentum is given by [4]

$$\frac{D\mathbf{v}_a}{Dt} = -\sum_{b=1}^{N} m_b \left(\frac{P_b \pm P_a}{\rho_a \rho_b} + \Pi_{(a,b)} \right) \nabla_{r_a} W(q_{ab}) + \mathbf{g} + \int_{S(t)} (\mathbf{v}(\mathbf{r}, t) \cdot \mathbf{n}) \mathbf{v}(\mathbf{r}, t) W(q_a) \, \mathrm{d}S - \frac{1}{\rho_a} \int_{S(t)} P(\mathbf{r}, t) W(q_a) \mathbf{n} \, \mathrm{d}S \tag{30}$$

in which $\Pi_{(a,b)}$ is an artificial viscosity introduced to improve numerical stability and to mimic physical viscosity. The subscript (a, b) indicates that the viscosity term has a functional dependence on the properties of both particles a and b. In the derivation of Equation (30) it is assumed that the kernel gradient operators are anti-symmetric and that the kernel itself is normalized. The boundary integrals that are usually neglected are the last two terms in Equation (30), the first of these coming from accounting for the time-dependent boundary in $\mathrm{d}\mathbf{v}_a/\mathrm{d}t$, and the second from using Gauss' law on the right-hand side.

The P_a term that appears in Equation (30) is zero in the limit as N approaches infinity, and so may be added or subtracted, hence the $\pm$. Monaghan [22] asserts that to use $-$ means linear momentum will not be conserved but that for constant pressures the gradient estimate is exact. It seems to us that an error is of less importance than the failure to conserve momentum, and so we use the form with $+$.

The form of the viscosity term is somewhat arbitrary and many different schemes have been proposed. The scheme used by Monaghan [4] in his paper describing simulations of breaking waves is

$$\Pi_{(a,b)} = -\frac{\lambda}{h} \frac{(c_a + c_b)}{(\rho_a + \rho_b)} \frac{(\mathbf{v}_a - \mathbf{v}_b) \cdot \mathbf{u}_{ab}}{(q_{ab}^2 + \eta)} \times \begin{cases} 1 & (\mathbf{v}_a - \mathbf{v}_b) \cdot \mathbf{u}_{ab} < 0 \\ 0 & (\mathbf{v}_a - \mathbf{v}_b) \cdot \mathbf{u}_{ab} > 0 \end{cases} \tag{31}$$

where c_a is the speed of sound for the particle a. The term η is added artificially to avoid singularities that occur whenever $q_{ab} = 0$, and generally $\eta = 0.01$. The quantity λ can be related to the kinematic viscosity of the fluid [23], but the value used depends upon the application [4], 0.01 being likely.

DOI: 10.1002/fld

A problem with this viscosity model is that it was designed to account for stability and shock capturing and it appears that it contributes to the unphysically dispersive nature of fluids in SPH simulations that use it [24]. More sophisticated techniques are required to accurately account for the turbulence in fluids [25].

2.2.6. Neglecting the boundary integrals. In Section 2.2.2, the SPH equation for conservation of mass was derived, and the lack of boundary integrals was noted. This is a convenient result but is not true for the SPH momentum equation (30).

If the position $\mathbf{r}_a$ is far enough from the boundary that $W(q_{ab})$ is zero for all points $\mathbf{r}_b$ on the boundary, or if the fluid property of interest is zero along the boundary, then the boundary integral is zero. For bounded, free surface fluid flows neither of these two conditions are satisfied for all particles.

The first boundary integral in (30) contains the term $\mathbf{v} \cdot \mathbf{n}$, and on stationary boundaries we can apply the zero mass flux boundary condition $\mathbf{v} \cdot \mathbf{n} = 0$, so these integrals may be neglected. However, not all boundaries are stationary. The free surface is a significant example of this, as are moving surfaces such as wave makers. The second boundary integral in (30) may be neglected on the free surface by an application of a zero-pressure boundary condition, but on other surfaces it is non-zero. The neglect of these surface integrals is not justified.

2.2.7. The error in the SPH equations. Using methods similar to those in Section 2.1.1 it is not too difficult to show that the discretized continuity equation (22) reduces to

$$\frac{D\rho_a}{Dt} = -\rho_a \sum_{b=1}^{N} \frac{\mathbf{u}_{ab}^{\mathrm{T}} J\mathbf{v}_a \mathbf{u}_{ab}}{q_{ab}} \frac{\mathrm{d}W(q_{ab})}{\mathrm{d}q_{ab}} \frac{m_b}{\rho_b} + O(h) + O(h \cdot f(N)) \tag{32}$$

in which $\mathbf{u}_{ab}$ is a column vector and $J\mathbf{v}_a$ is the Jacobian of $\mathbf{v}_a$ which has terms independent of b. Also, we have used the fact that

$$\nabla_{r_a} W(q_{ab}) = -\frac{\mathbf{u}_{ab}}{h q_{ab}} \frac{\mathrm{d}W(q_{ab})}{\mathrm{d}q_{ab}} \tag{33}$$

It is useful to define the matrix

$$E = -\sum_{b=1}^{N} \frac{\mathbf{u}_{ab} \otimes \mathbf{u}_{ab}}{q_{ab}} \frac{\mathrm{d}W(q_{ab})}{\mathrm{d}q_{ab}} \frac{m_b}{\rho_b} \tag{34}$$

in which $\otimes$ is the outer (or tensor) product. If $[J\mathbf{v}_a]_{ij}$ is the ijth term of $J\mathbf{v}_a$ then Equation (32) can be rewritten as

$$\frac{D\rho_a}{Dt} = \rho_a \sum_{i=1}^{d} \sum_{j=1}^{d} [J\mathbf{v}_a]_{ij} E_{ij} + O(h) + O(h \cdot f(N)) \tag{35}$$

In the limit as $N \to \infty$ the $O(h \cdot f(N))$ error tends to zero and $E \to I$, meaning the summation in Equation (35) is equal to $\nabla_{r_a} \cdot \mathbf{v}_a$ so we have

$$\frac{D\rho_a}{Dt} = -\rho_a \nabla_{r_a} \cdot \mathbf{v}_a + O(h) \tag{36}$$

Both of the terms $O(h)$ and $O(h \cdot f(N))$ in Equation (32) have factors of the first and second derivatives of ρ and $\mathbf{v}$ and so are zero if ρ and $\mathbf{v}$ are constants, in which case the estimate is

DOI: 10.1002/fld

zeroth-order complete. In general, however, $E \neq I$ and the $O(h)$ and $O(h \cdot f(N))$ errors are less significant than the non-unitary factor multiplying $\nabla_{r_a} \cdot \mathbf{v}_a$. The error introduced by this factor may be characterized by the determinant of E, a measure of the failure to achieve zeroth-order completeness.

The SPH momentum equation is actually easier to deal with than that for mass in this analysis. It is useful to define the vector

$$\mathbf{d} = \sum_{b=1}^{N} \frac{\mathbf{u}_{ab}}{q_{ab}} \frac{\mathrm{d}W_{ab}}{\mathrm{d}q_{ab}} \frac{m_b}{\rho_b} \tag{37}$$

Starting with (30) and by neglecting the boundary and viscosity terms for simplicity and performing a Taylor expansion on P_b, it can be shown that

$$\frac{D\mathbf{v}_a}{Dt} = -\frac{1}{\rho_a} \sum_{b=1}^{N} \left(\pm P_a + P_a + \nabla^{\mathrm{T}} P_a (\mathbf{r}_a - \mathbf{r}_b) + \frac{1}{2} (\mathbf{r}_a - \mathbf{r}_b)^{\mathrm{T}} [H P(\boldsymbol{\xi}, t)] (\mathbf{r}_a - \mathbf{r}_b) \right) \times \frac{\mathbf{u}_{ab}}{h q_{ab}} \frac{\mathrm{d}W(q_{ab})}{\mathrm{d}q_{ab}} \frac{m_b}{\rho_b} + \mathbf{g} \tag{38}$$

where the Lagrangian form for the remainder has been used. This simplifies to

$$\frac{D\mathbf{v}_a}{Dt} = -\frac{\nabla^{\mathrm{T}} P_a}{\rho_a} E - (1 \pm 1) \frac{1}{h} \frac{P_a}{\rho_a} \mathbf{d} + \mathbf{g} + O(h) + O(h \cdot f(N)) \tag{39}$$

The (1 ± 1) factor relates to the $\pm P_a$ appearing in Equation (30). The benefit in using the $-$ form means that (1 ± 1) is identically equal to zero, while if the $+$ form is used this error term dominates, actually diverging with h. We characterize this error by $|\mathbf{d}|$. In the limit as $N \to \infty$, $\mathbf{d} \to \mathbf{0}$ and $E \to I$ so

$$\frac{D\mathbf{v}_a}{Dt} = -\frac{\nabla P_a}{\rho_a} + \mathbf{g} + O(h) \tag{40}$$

irrespective of which form is used. If we were to use the $-$ form then, like the mass equation, the error is determined by the deviation of E from I. However, we still need to use the $+$ form because the $-$ form results in the non-conservation of momentum [9].

2.2.8. Conservation of energy. For a system with constant temperature the principle of conservation of energy is not independent of the principles of conservation of mass and momentum. As such, energy conservation is achieved automatically, without being enforced, but still provides a useful and intuitive method for checking the model is behaving reasonably. The total energy for particle a is given by

$$e_a = m_a u_a + \tfrac{1}{2} m_a v_a^2 + m_a g z_a + m_a \Phi_a + m_a e_{\Pi,a} \tag{41}$$

in which the terms are the internal, kinetic, gravitational and boundary potential energies, and the energy dissipated by viscosity, respectively. Here g is the acceleration due to gravity, z_a is the height of the particle with respect an arbitrary reference level and the boundary force for particle

DOI: 10.1002/fld

a is found from the gradient of Φ_a, the boundary potential. The specific internal energy of each particle can be calculated from [4]

$$\frac{Du_a}{Dt} = \frac{1}{2}\sum_{b=1}^{N} m_b \left(\frac{P_a}{\rho_a^2} + \frac{P_b}{\rho_b^2}\right)(\mathbf{v}_a - \mathbf{v}_b)\cdot\nabla_{r_b} W(q_{ab}) \tag{42}$$

or by integrating the definition for pressure, $\mathrm{d}u/\mathrm{d}\rho = P/\rho^2$ [26], with respect to ρ from a reference density to ρ_a. The viscous dissipation is given by [4]

$$\frac{De_{\Pi,a}}{Dt} = \frac{1}{2}\sum_{b=1}^{N} m_b \Pi_{(a,b)}(\mathbf{v}_a - \mathbf{v}_b)\cdot\nabla_{r_b} W(q_{ab}) \tag{43}$$

which may be integrated over time using any time-stepping method. Here we use a two-stage predictor–corrector technique.

Global conservation of energy requires that the global energy ($\sum_{a=1}^{N} e_a$) be constant in time for a closed system. This provides a useful check for gross errors in the source code, and for the quality of a simulation.

2.2.9. Conservation of angular momentum. If a system contains a number of particles which are subject to Newton's third law, and forces between each pair of particles are central (they act in the same direction as the vector separating the particles) then the equation of conservation of angular momentum can be derived. But not all forces (magnetic and viscous, for example) are central, and when this condition is relaxed the equation of conservation of angular momentum is independent of the equations of conservation of mass and momentum and can no longer be derived. However, in most SPH applications this is not accounted for, and this paper is no different.

As such conservation of angular momentum is rather like conservation of energy in that it is not required but provides a useful method for identifying mistakes in source code and perhaps quantifying the quality of a simulation. We stress the point that here we test for global conservation of angular momentum obtained from

$$T = \sum_{a=1}^{N} m_a \mathbf{r}_a \times \mathbf{v}_a \tag{44}$$

2.2.10. Updating positions and the XSPH variant. Monaghan [27] introduced the XSPH variant to improve the simulation of fluids with free surfaces. Essentially, this term performs velocity smoothing. Rather than using Equation (17) for updating particle positions we use

$$\frac{\mathrm{d}\mathbf{r}_a}{\mathrm{d}t} = \mathbf{v}_a + \varepsilon\sum_{b=1}^{M} \frac{2m_b(\mathbf{v}_a - \mathbf{v}_b)W(q_{ab})}{\rho_a + \rho_b} \tag{45}$$

in which the factor $0 \leqslant \varepsilon < 1$ is an arbitrary parameter. In this work wherever XSPH is used we take $\varepsilon = 0.5$.

3. MODEL RESULTS

Vaughan [28] developed an SPH model that is used here to generate results which demonstrate various types of error that occur in SPH simulations. The discretized continuity equation is used for

DOI: 10.1002/fld

enforcing conservation of mass rather than the summation interpolant for the density. Boundaries are created using the method described by Monaghan [4] where boundary points are specified whose sole role is to exert a force on free particles—they have no mass and carry no energy. The time-stepping method is a two-stage predictor–corrector. Pressure is calculated from the equation of state used by Monaghan [4], which means the fluid is arbitrarily compressible. First-order completeness can be achieved optionally in the calculation of property gradients by the kernel gradient correction [8]. XSPH [27] can also be used if desired. Having just argued that boundary integrals should not be neglected that is exactly what we do here. The difficulty lies in identifying where exactly the boundaries are and what their velocities are. This problem is not trivial and is not solved here.

The first simulation we describe is the evolution of an elliptic drop. In this simulation the improvements achieved by correcting for completeness are demonstrated, namely reduced variations in density and smoother surfaces. We also show the non-conservation of global energy in simulations corrected for completeness.

A seiche in a rectangular basin is simulated, demonstrating the consequences of the choice for the kernel made here, and particle stacking, an example of a discretization error. Finally, breaking waves on plane-sloped beaches are simulated, and an interesting feature of the flow is noted: toothpaste jets, which are unphysical jets within boundary layers.

3.1. The evolution of an elliptic drop

Monaghan [4] described a relatively simple simulation, the evolution of an elliptic drop, that has since been examined by Bonet and Lok [7] and by Vaughan [28]. Essentially, we create a two-dimensional circular drop of water from SPH particles, and we specify initial particle velocities chosen so that the drop remains elliptic in time, getting longer and narrower.

The merit in repeating this simulation here is that it provides a useful comparison against both a sound theoretical result, and against results from other SPH models. Accurate numerical solutions for the semi-minor and semi-major axes can be readily obtained and compared to the SPH simulation.

The simulations performed here follow closely the method used by Monaghan [4]. Points are placed on the vertices of a rectangular grid, and all those lying outside a circle (radius 1, centred at the origin) are removed, leaving a total of 1884. Initial velocities are linear in space, given by

$$(v_x, v_y) = 100(-r_x, r_y) \tag{46}$$

The density of the water is taken as $1000\,\mathrm{kg\,m^{-3}}$ and artificial viscosity is not used. The reference speed of sound is $1400\,\mathrm{m\,s^{-1}}$ (slightly less than the measured value of around $1500\,\mathrm{m\,s^{-1}}$), chosen in an attempt to keep density variations low. The full set of results for these simulations appear in Vaughan [28].

3.1.1. Particle positions. The same initial state was used to generate four simulations, each using different parameters, namely, using SPH without modifiers, using SPH with XSPH, using SPH with a kernel gradient correction (CSPH, see Equation (11)), and lastly using the kernel gradient correction and the XSPH variant to get CXSPH. Figure 2 shows particle positions from each of the simulations at the same time. It is clear that the SPH simulation has by far the least evenly distributed particle positions. Close examination reveals that distributions are more even in the XSPH simulation, CSPH even more so and CXSPH the best of all. There is not a lot of difference

DOI: 10.1002/fld

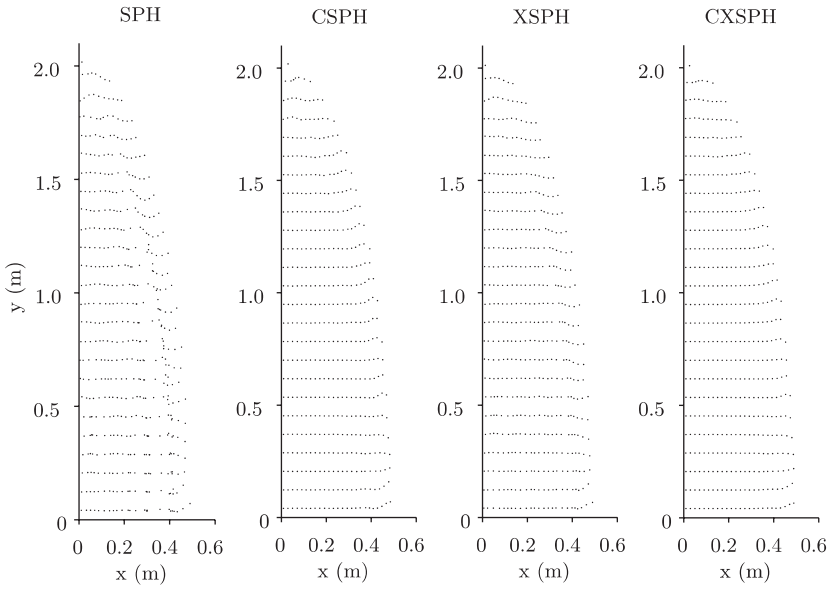

Figure 2. The effects of the XSPH and CSPH variants on the evolution of an elliptic drop. Particle positions are shown at $t = 8.2$ ms. Only the top right quarter of each ellipse is shown for clarity, the other quarters being rather similar. Particle distributions are far more regular for CSPH and XSPH than for SPH, but the CXSPH simulation is the best of all.

between the best three, however, and it is not entirely clear that more uniform particle distributions indicate a more accurate simulation.

3.1.2. The semi-major axis. Here, we estimate the semi-major axis from the positions of the highest and lowest particles. This approach is somewhat sensitive to fluctuations in the positions of these particles, but provides sufficiently good results. Figure 3 contains a plot of errors in values for the semi-major axis taken from the simulations performed here, along with values taken from both Monaghan [4] and Bonet and Lok [7]. The error is given by

$$100\frac{(b - b_{\text{sim}})}{b} \tag{47}$$

in which b is the value of the semi-major axis from theory and b_{sim} is the value from which ever simulation is being examined.

There are slight differences in the models used to generate Figure 3. It is not clear whether Monaghan [4] used XSPH or viscosity to obtain his simulations, and the time-stepping methods are not the same for all models, since Bonet and Lok [7] used a leap-frog method, and while Monaghan [4] used the same predictor–corrector method used here, he updated the velocity before the density (the opposite to the procedure used here). Notably, Bonet and Lok [7] used a different initial state (points placed regularly on the boundary of a unit circle and randomly but evenly distributed within the circle). It is relatively easy to estimate the error introduced by the failure to have a point lying on the y-axis, and it is found to be less than 0.05% for all times. This is not significant and actually improves the results of the simulations run here.

DOI: 10.1002/fld

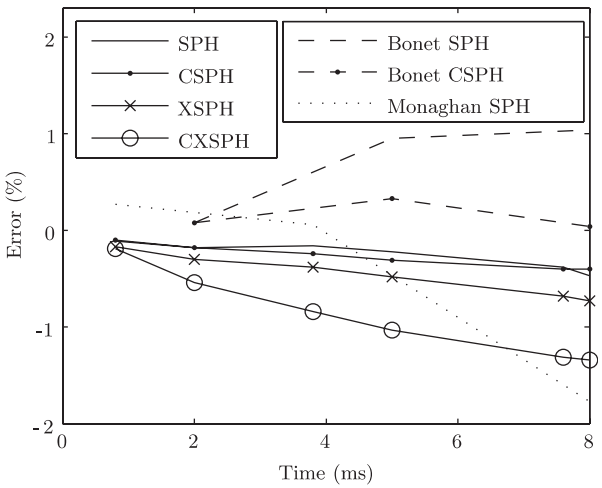

Figure 3. Error in values of the semi-major axis for the elliptic drop simulations. The error is the deviation from the exact value, expressed as a percentage difference, from Equation (47). The data marked Bonet and Monaghan are from Bonet and Lok [7] and Monaghan [4], respectively. Simulations from all sources show errors of similar magnitude.

Clearly, simulations from all of the different sources show errors of similar magnitude. Of the simulations performed here it is somewhat surprising that the most accurate estimate for the semi-major axis was obtained using SPH. That other tests of accuracy (discussed in the following sections, they are maximum variation of density and conservation of energy) show the SPH simulation to be poor lead us to conclude that estimates of the semi-major axis cannot be used as the sole indicator of error.

3.1.3. Variation in density. Monaghan [4] estimates the magnitude of the variation in density to be

$$\frac{\delta\rho}{\rho} \approx \frac{v_{\max}^2}{c_{\text{ref}}^2} \tag{48}$$

Here $c_{\text{ref}} = 1400\,\text{m}\,\text{s}^{-1}$ is the reference speed of sound and $v_{\max} = 100\,\text{m}\,\text{s}^{-1}$ is the maximum likely velocity, so the maximum density variation is 0.5%. Figure 4 shows the maximum density (the largest difference from $1000\,\text{kg}\,\text{m}^{-3}$ as a percentage, $100 \times |\rho_{\max} - 1000|/1000$) against time. Notable are the excellent results from the CSPH and CXSPH simulations, in which the maximum density variations are almost constant. The variations for both the XSPH and SPH simulations grow almost linearly, at a much higher rate in the SPH simulation. For the SPH simulation (as can be seen in Figure 2), and to a lesser extent for the XSPH simulation, artificial clustering can be seen. This is a likely cause for the high variability in the density in these simulations.

3.1.4. Global conservation of energy and angular momentum. Figure 5 shows the global total, internal and kinetic energies (gravity is turned off) for the system. In all of the simulations a periodic exchange of energy between the internal and kinetic modes can be observed, a result of the compressibility of the fluid. For the XSPH and SPH simulations the global total energy

DOI: 10.1002/fld

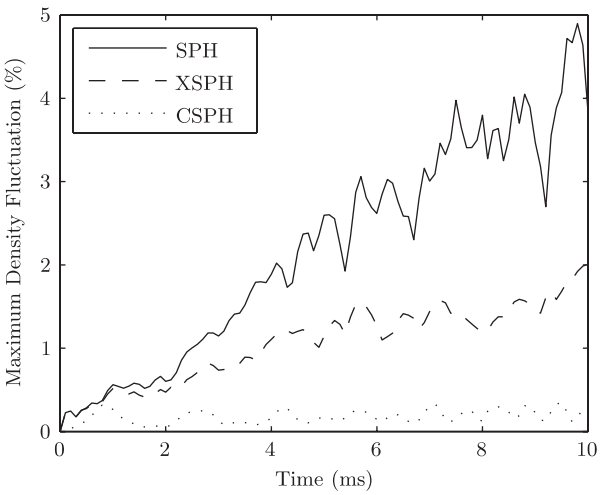

Figure 4. The maximum deviation of density from the standard density ($1000\,\mathrm{kg\,m^{-3}}$) as a percentage, for the elliptic drop simulations. Curves for CSPH and CXSPH are indistinguishable and remain safely under the predicted 0.5%.

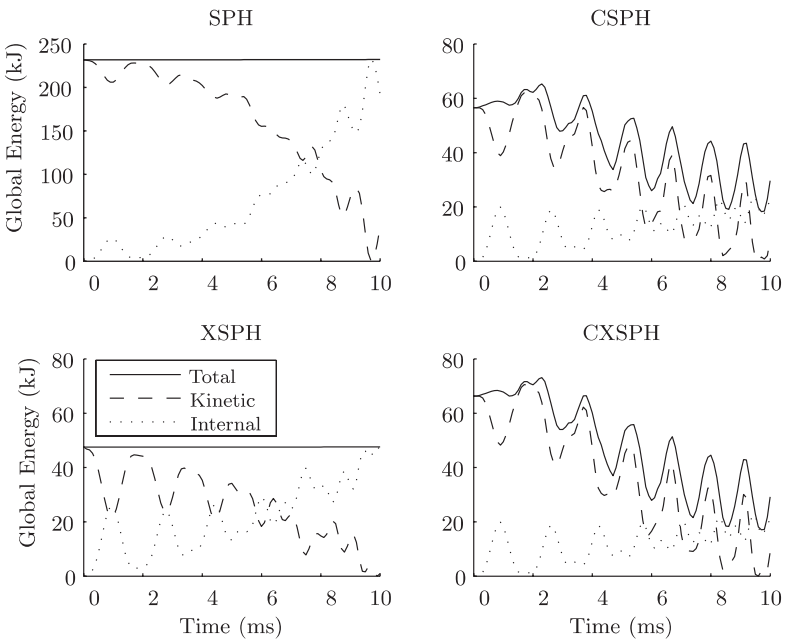

Figure 5. The global total, internal and kinetic energies against time for each of the elliptic drop simulations. Note the different vertical scale of the SPH plot. In CSPH and CXSPH global energy is not conserved, a significant problem.

DOI: 10.1002/fld

is conserved almost exactly since the corresponding curves are straight, horizontal lines. For the CSPH and CXSPH simulations global energy is not conserved, and so energy is not conserved locally either, a significant problem. This substantiates our assertion that the errors introduced by using kernel gradient correction result in the failure to satisfy the conservation principles.

3.1.5. Local errors in the SPH equations. In Section 2.2.7 quantities were given that describe the magnitude of errors in the SPH equations, being $\det(E)$ and $|\mathbf{d}|$. The closer these are to 1 and 0, respectively, the closer the gradient estimate to being zeroth-order complete. In the CSPH and CXSPH simulations $E = I$ and $\mathbf{d} = \mathbf{0}$ exactly, but for those methods E and $\mathbf{d}$ do not describe the error.

In Figure 6 we show $\log_{10}(|\mathbf{d}|)$ for the XSPH simulation (results for the SPH simulation are similar but slightly worse). Data for $\det(E)$ are similar and are not shown here. For the majority of particles the error is smaller than 10^{-1}, but a significant number have an error greater than 1. That the worst errors occur at the surface is problematic.

3.1.6. Concluding remarks on the elliptic drop simulations. The results presented here indicate that the model completed the elliptic drop simulation to an acceptable level, and compares well to other SPH models in the literature.

Density variations and particle distributions are best for the CSPH and CXSPH simulations, worse for XSPH and worst of all for SPH. Distributions in the initial states are regular and should remain so, and consequently failure in this should be considered symptomatic of the occurrence of error. As to what is acceptable variation in density is an issue of tolerance (variation may be reduced by enforcing a higher speed of sound) and does not represent and absolute rule for accuracy, but the trend of variation increasing far beyond the anticipated limits in SPH and XSPH simulations is a definite problem.

Global energy is conserved in the SPH and XSPH simulations but is not when CSPH or CXSPH are used, a major problem.

For SPH and XSPH the fact that $E \neq I$ and $\mathbf{d} \neq \mathbf{0}$ mean errors are high, especially at surfaces, and can be attributed to the lack of completeness.

Ideally, the best attributes of both CSPH and SPH would be combined to create a complete and conserving SPH method, but this will not be achieved here. The failure to conserve energy represents a far more fundamental concern than large errors, poor particle distributions and high-density variations. From this point on CSPH and CXSPH are not used.

3.2. A seiching basin

This is a simple simulation we used extensively in the development of our model, because it runs to completion quickly, but still has many interesting features. The simulation is simply a rectangular basin containing still water with an initially sinusoidal free surface that is allowed to evolve. The amplitude of the wave is too high to be considered a linear wave and it is not likely that the wave is permanent (does not change shape as it propagates), but we can anticipate that the basin will seiche for a number of times before the wave energy disperses and the seiche amplitude drops.

The basin is approximately 90 m long and 13 m deep, and is initialized with a sinusoidal wave with a 180 m wavelength, shown in Figure 7. Particles are placed at the vertices of a rectangular grid and those above the sinusoidal free surface are discarded, leaving 2994 free fluid particles. The

DOI: 10.1002/fld

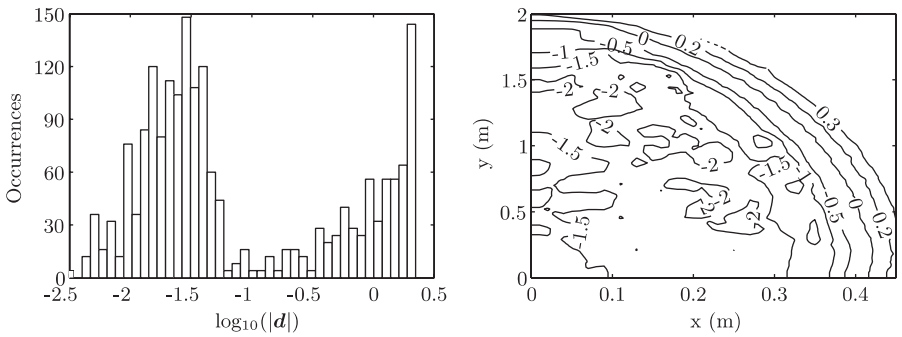

Figure 6. Errors in the XSPH simulation of the elliptic drop at 8.2 ms. On the left the distribution of values of $\log_{10}(|\mathbf{d}|)$ for all particles is shown, a measure of the leading error term in the SPH momentum equations (30). A contour plot of $\log_{10}(|\mathbf{d}|)$ for one quarter of the domain is shown in the right-hand plot. Clearly the error is largest at the edges of the drop. Note the distorted axes ratio used for clarity in the right-hand plot.

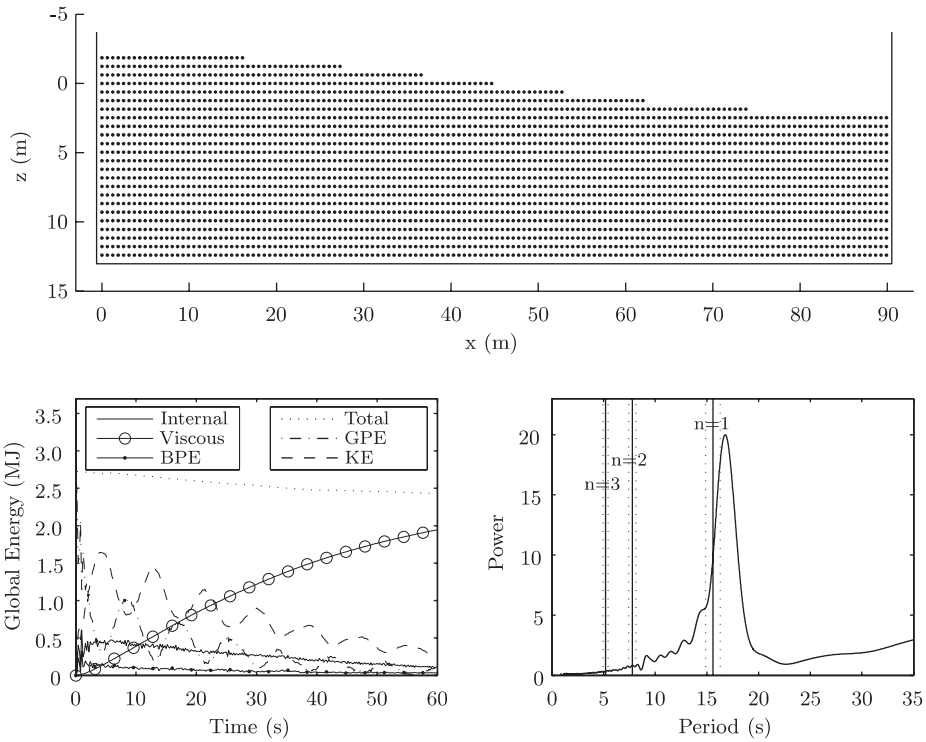

Figure 7. The initial state of the seiching basin (top) using 2994 points with all velocities set to zero. The global energies are shown in the bottom left plot. The time between two adjacent energy maxima is half a seiche period. The bottom right plot shows the spectrum obtained from the gravitational potential energy. The full vertical lines are the periods for the first three modes predicted from Merian's formula and the dotted lines show the associated uncertainties.

DOI: 10.1002/fld

density is $1000\,\mathrm{kg\,m^{-3}}$ and particles are initialized with zero velocity. Viscosity is used (Equation (31)) with $\lambda = 5 \times 10^{-4}$, the time step is 0.5 ms, the smoothing length is 2 m. Using the XSPH variant did not improve results significantly and is not used. A more extensive set of results is available in Vaughan [28].

3.2.1. Global conservation of energy. In Figure 7 the global energies are shown for the seiching basin. The periodic exchange between kinetic and gravitational potential energies is evident, as is the decreasing amplitude of the seiche, for the most part a result of the poor viscosity model used. Note the increasing amount of energy dissipated by viscosity and that there are only small variations in boundary potential energy. Like the gravitational potential energy, the internal and boundary potential energies are relative, and are plotted here so that their lowest value is zero. This means all global relative energies are positive and plots accentuate the variation in energy, rather than the actual value found for some other arbitrary reference level.

It can also be seen that there is an early drop (between 0 and 2 s) in the gravitational potential energy, predominantly caused by artificial clustering that occurs early in the simulation along the bottom boundary. That the global total energy is not constant is a result of the accumulation of numerical errors, most significantly those resulting from time stepping.

3.2.2. Merian's formula. Merian's formula

$$T = \frac{2L}{n\sqrt{gH}} \tag{49}$$

gives the periods for linear modes in a seiching basin. The fundamental mode corresponds to $n = 1$ which is specified in the initial state. The mass (and hence surface) of a single particle has an unknown distribution, and so the free surface of the fluid and the positions where it meets the boundaries are not specified by sharp interfaces. This means there is some uncertainty as to the values for length and depth that are required here. Here, we specify the length to be 90.63 ± 0.51 m and the depth to be 13.78 ± 1.24 m. The period of the nth mode is $15.59/n \pm 0.71/n$ s.

The period of the seiche can be determined by examining the global gravitational potential energy, and performing a fast Fourier transform. A spectrum generated in this way is shown in the right-hand plot of Figure 7. The peak in the spectrum corresponding to the fundamental frequency is indicated, and has a period of 16.76 s. The peak of the spectrum is in close agreement with the value from Merian's formula, but occurs at a higher period. This is partly a result of crystallized states.

3.2.3. Crystallized states. Crystallized states occur in SPH simulations as approximately triangular arrays of particles. Essentially, given the chance, particles will stack on each other like oil drums. These states were observed and named by Lombardi *et al.* [11] who termed the tendency of particle distributions in SPH to enter these states as spurious transport of energy. These states can be observed in the simulations here as small features (approximately 10 particles) which do not flow as they should.

Figure 8 shows a simulation in which the particles are in a crystallized state. Here the fluid has been discretized with particles of 2666 kg, has a density of $1000\,\mathrm{kg\,m^{-3}}$, the speed of sound is $1500\,\mathrm{m\,s^{-1}}$, and the smoothing length is 0.9 m. Particles are initially 3 m from their nearest neighbours so the stack is around 8 m high. Artificial viscosity is not used and gravity is turned on. It is essentially a triangular distribution of particles for which the kinetic energies have been

DOI: 10.1002/fld

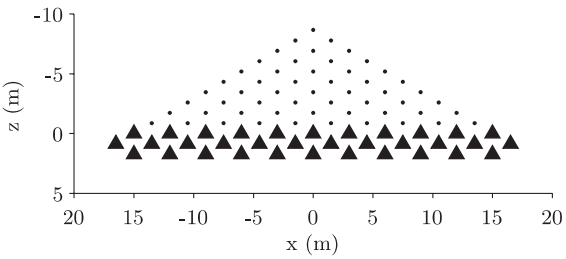

Figure 8. The initial state of the stacking simulation. Three rows of boundary particles (the triangles) were found to be required in order that particles be constrained. Particles are stable in these positions for a considerable time. The fluid fails to flow because particles are in a crystallized state.

smoothed, and once started, the simulation stays in its initial state for some time. Eventually numerical errors accumulate and a few particles gain enough energy to escape the stack. This simulation shows that crystallized states occur in fluid simulations and can cause clearly unphysical manner.

The simulation used to generate Figure 7 had particles initially distributed on a rectangular grid. To emphasize the role of crystallized states, the seiching basin simulation was re-run with particles initially placed on a triangular grid. Three rows of boundary particles were used to ensure particles did not leak through. Particle positions are shown for one time step in Figure 9. Note the sloping parallel lines of particles that occur at the bottom of the basin; lines which swap direction as the seiche oscillates from one side to the other. This is a result of particles entering into crystallized states.

In Figure 9 the interpolated velocity profiles along a vertical line at the centre of the basin ($x = 45$m) are plotted for a number of times, with each curve being shifted along the x-axis. The zero-velocity curves are shown by the dashed lines. For each time the velocities predicted from linear wave theory [29] are also shown (the chained lines), and clearly these vary only slightly from being constant with depth. The boundary layer caused by crystallized states can be seen at the bottom, where velocity profiles do not portray expected behaviour.

In the seiching basin with initially rectangularly distributed points crystallized states are less likely, however, they may still be present. If they are, they will cause a decrease in the apparent depth, increasing the periods of the modes. Note that in Figure 7 the period predicted by Merian's formula is lower than that observed in the simulation. Crystallized states are not the only mechanism by which layers are formed at boundaries of SPH simulations, but may contribute to the high seiche period observed here.

3.3. Numerical layers at boundaries and toothpaste jets

In this section, we briefly examine toothpaste jets, a surprising feature that can occur in some SPH simulations. Monaghan [4] observed layers beside boundaries in some simulations, but these remain unexplained. They can be avoided by using kernels with monotonically decreasing gradients (because they are, in part, caused by artificial clustering), but they are an interesting result.

Figure 10 shows the initial state (top) of a solitary wave incident on a plane beach with slope 1:15, drawn from a simulation that features these layers. The surface elevation and initial velocities

DOI: 10.1002/fld

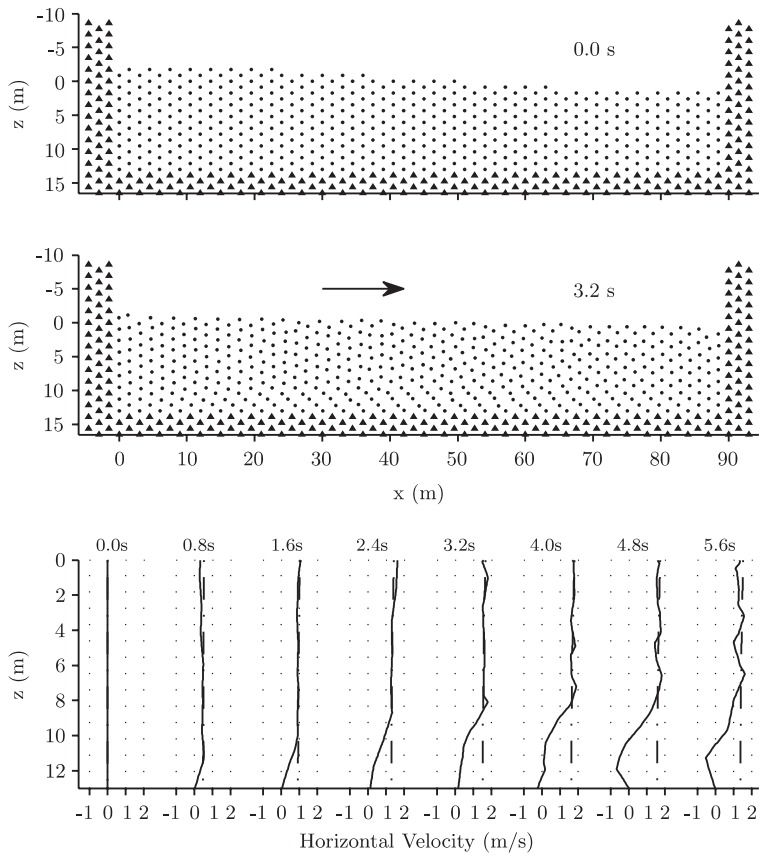

Figure 9. The seiching basin with an initially triangular distribution of points (top), in which the fluid particles are the dots and the boundary points are the triangles. At 3.2 s (centre) a stagnant layer has formed at the lower boundary. In this plot the direction of the flow is shown by the arrow. The bottom plot shows velocities interpolated along the line at $x = 45$ m. For each time the velocity curve from the simulation (the full line) has been shifted along the x-axis, as have the chained lines which show the velocities predicted by linear wave theory.

are obtained using a second-order solitary wave solution [30]. The layer at the boundary is evident in the central plot, as a layer of closely packed particles next to the beach. The arrows are the velocity vectors of particles within this layer, and show the existence of a jet within the layer. The layer is not physical, and should not be called a boundary layer which would confuse it with the real physical phenomenon.

The layer is a result of the compressibility of fluids in SPH. In order that a pressure gradient be generated that opposes gravity, a density gradient must be generated. Whether the densities of particles must increase or decrease depend on whether the densities in the initial state are under- or over-estimated. In order that the density increase at any particular point, the particles must become more closely packed. Where a particle has many neighbours each needs only to move a relatively small distance to cause an increase in the density, but where a particle has few neighbours

DOI: 10.1002/fld

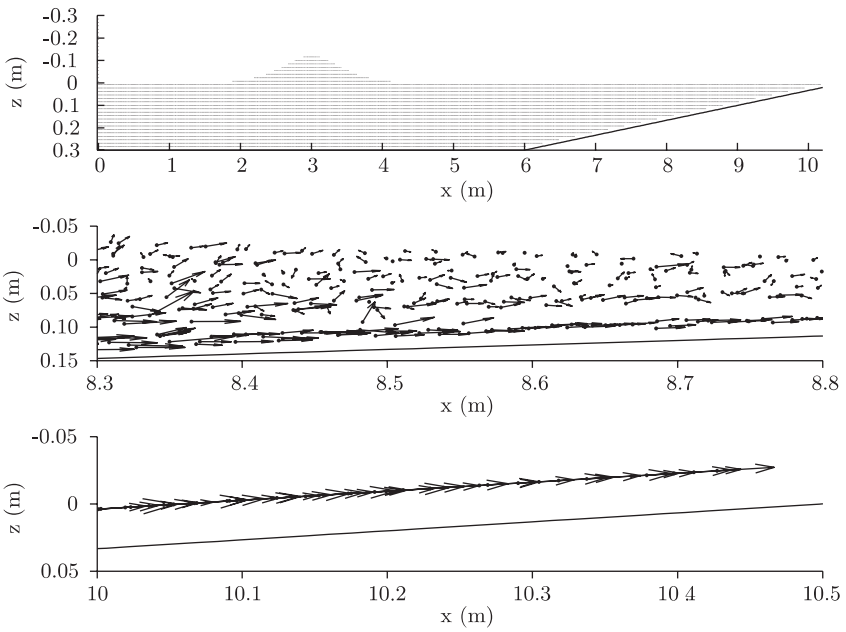

Figure 10. The initial particle positions (top) for the solitary wave simulation. The free surface and velocities are prescribed using a second-order solution [30]. The lower two plots show detail of particle velocities at 2.4 s when the peak of the wave is at 7.7 m. The unphysical layer next to the boundary is clear in the middle plot, and it is within this layers that a toothpaste jet can be seen, causing the flow up the beach in the lowest plot. The velocity vectors in the lower plot are shown at a larger scale than that used in the centre plot.

they must move much more. Essentially, gravitational potential energy is transformed to become internal (compressive) energy.

The greatest increases in density are required by particles adjacent to the bottom, where the number of neighbours drops sharply because there is less fluid within the supports of those particles. Where particles are more closely packed they are more likely to cluster. So the layer can be considered as being a single, long, cluster. But where clusters can still move (they behave as super-particles with high mass and density) the near-wall layer is constrained to remain next to the boundary. Indeed, if the boundary were not there they would not have formed.

The weight of the moving wave crest causes a region of high pressure at the sea floor. As the wave crest propagates towards the beach so too does the high-pressure zone, progressively squeezing the layer. Being constrained to remain within the layer, this squeezing results in particles being accelerated horizontally within the layer, rather like toothpaste being squeezed from a tube: toothpaste jets.

These jets affect this simulation in two ways. Firstly, they cause the acceleration of a thin layer of particles up the slope, well ahead of the wave. This means estimates of wave run-up are difficult to make. Secondly, with the smoothing that is the means by which SPH works, they provide a mechanism by which momentum is passed from under the wave crest to the toe of the wave, disrupting the breaking process.

DOI: 10.1002/fld

4. DISCUSSION AND CONCLUSIONS

We have revisited the error analysis of the SPH interpolant that provides the basis for discretization in SPH and have derived expressions for the error that depend on the degree of completeness that is achieved. If zeroth-order completeness is not achieved the error is $O(f(N))$, which does not converge with h, whereas if first-order completeness is achieved the error is $O(h^2 \cdot f(N))$. An SPH estimate may converge at any chosen rate but the degree of completeness achieved determines the number of computations required. For the SPH equations we find that the errors are $O(h^{-1} \cdot f(N))$ and $O(h \cdot f(N))$ for the cases of not-zeroth and first-order complete kernels, respectively. This result emphasizes the importance of completeness.

When derived by the standard method, if the time dependence of the model domain is accounted for, the SPH equation for mass conservation has no boundary integrals, a useful result given that they are always neglected. It turns out that the summation interpolant for density is a solution to the discretized mass conservation equation. The boundary integrals for the SPH momentum equation do not cancel and cannot obviously be neglected but they are nonetheless. We show that, in the course of deriving the SPH equations, an anti-symmetry condition for the two gradient operators acting on the kernel arises. A method by which completeness may be enforced results in the violation of the fundamental conservation principles because this condition is not satisfied. A complete and conserving SPH would be useful.

We present results that demonstrate how discretization errors can cause features in simulations far larger than the scale at which they originate. In particular, we show that crystallized states may be present in fluid simulations meaning that stagnant pockets and layers occur. An explanation is provided for the occurrence of numerical boundary layers that have been observed in some simulations. We show evidence of a previously unseen effect, where an unphysical jet exists within this layer, significantly influencing the behaviour of the system. Avoiding these layers and jets is as simple as using a kernel with a monotonically decreasing gradient.

ACKNOWLEDGEMENTS

The authors are grateful to the reviewers for their observations which have resulted in a greatly improved manuscript. G. L. Vaughan wishes to acknowledge the support of a PhD scholarship awarded by the University of Waikato.

REFERENCES

1. Gingold RA, Monaghan JJ. Smoothed particle hydrodynamics: theory and application to non-spherical stars. *Monthly Notices of the Royal Astronomical Society* 1977; **181**:375–389.
2. Lucy LB. A numerical approach to the testing of the fission hypothesis. *Astronomical Journal* 1977; **82**:1013–1024.
3. Jensen PS. Finite difference techniques for variable grids. *Computers and Structures* 1972; **2**:17–29.
4. Monaghan JJ. Simulating free surface flows with SPH. *Journal of Computational Physics* 1994; **110**:399–406.
5. Koshizuka S, Tamako H, Oka Y. A particle method for incompressible viscous flow with fluid fragmentation. *Computational Fluid Dynamics Journal* 1995; **4**:29–46.
6. Tang D, Yang C, Kobayashi S, Ku DN. Generalized finite difference method for 3-d viscous flow in stenotic tubes with large wall deformation and collapse. *Applied Numerical Mathematics* 2001; **38**(1–2):49–68.
7. Bonet J, Lok TSL. Variational, momentum preservation aspects of smooth particle hydrodynamic formulations. *Computer Methods in Applied Mechanics and Engineering* 1999 **180**:97–115.
8. Bonet J, Kulasegaram S, Rodriguez-Paz MX, Profit M. Variational formulation for the smooth particle hydrodynamics (SPH) simulation of fluid and solid problems. *Computer Methods in Applied Mechanics and Engineering* 2004; **193**:1245–1256.

DOI: 10.1002/fld

9. Monaghan JJ. Why particle methods work. *SIAM Journal on Scientific and Statistical Computing* 1982; **3**:422–433.
10. Belytschko T, Krongauz Y, Organ D, Fleming M, Krysl P. Meshless methods: an overview and recent developments. *Computer Methods in Applied Mechanics and Engineering*, *Special Issue on Meshless Methods* 1996; **139**:3–47.
11. Lombardi JC, Sills A, Rasio FA, Shaprio SL. Tests of spurious transport in smoothed particle hydrodynamics. *Journal of Computational Physics* 1999; **152**:687–735.
12. Monaghan JJ, Lattanzio JC. A refined particle method for astrophysical problems. *Astronomy and Astrophysics* 1985; **149**:135–143.
13. Niederreiter H. *Random Number Generation and Quasi-Monte Carlo Methods*. Society for Industrial and Applied Mathematics: Montpelier, Vermont, 1992.
14. Monaghan JJ. Particle methods for hydrodynamics. *Computer Physics Reports* 1985; **3**:71–124.
15. Quinlan NJ, Basa M, Lastiwka M. Truncation error in mesh-free particle methods. *International Journal of Numerical Methods in Engineering* 2006; **66**:2064–2085.
16. Schussler M, Schmitt D. Comments on smoothed particle hydrodynamics. *Astronomy and Astrophysics* 1981; **97**(2):373–379.
17. Swegle JW, Hicks DL, Attaway SW. Smoothed particle hydrodynamics stability analysis. *Journal of Computational Physics* 1995; **116**:123–134.
18. Monaghan JJ. SPH without a tensile instability. *Journal of Computational Physics* 2000; **159**:290–311.
19. Ferziger JH, Perić M. *Computational Methods for Fluid Dynamics*. Springer: Berlin, 1996.
20. Anderson JJ. *Computational Fluid Dynamics. The Basics with Applications*. McGraw-Hill: New York, 1995.
21. Adams RA. *Calculus of Several Variables* (4th edn). Addison-Wesley: Ontario, 1999.
22. Monaghan JJ. Smoothed particle hydrodynamics. *Annual Review of Astronomy and Astrophysics* 1992; **30**: 543–574.
23. Monaghan JJ, Kos A. Solitary waves on a Cretan beach. *Journal of Waterway*, *Port*, *Coastal and Ocean Engineering* 1999; **125**(3):145–154.
24. Rogers BD, Dalrymple RA. SPH modelling of breaking waves. *Proceedings of the 29th International Conference on Coastal Engineering*, Lisbon, Portugal. ASCE: New York, 2004; 415–427.
25. Violeau D, Issa R. Numerical modelling of complex turbulent free-surface flows with the SPH method: an overview. *International Journal of Numerical Methods in Fluids* 2007; **53**:277–304.
26. Lu PC. *Fluid Mechanics*: *An Introductory Course*. Iowa State University Press: Ames, Iowa, 1979.
27. Monaghan JJ. On the problem of penetration in particle methods. *Journal of Computational Physics* 1989; **82**:1–15.
28. Vaughan GL. Simulating breaking waves using smoothed particle hydrodynamics. *Ph.D. Thesis*, University of Waikato, Hamilton, New Zealand, 2005.
29. Mei CC. *The Applied Dynamics of Ocean Surface Waves*. World Scientific: Singapore, 1989.
30. Dean RG, Dalrymple RA. *Water Wave Mechanics for Engineers and Scientists*. Advanced Series on Ocean Engineering, vol. 2. World Scientific: Singapore, 1991.

DOI: 10.1002/fld